

Machine-learning Accelerated Descriptor Design for Catalyst Discovery: A CO₂ to Methanol Conversion Case Study

Prajwal Pisal^{1†}, Ondřej Krejčí^{1†}, Patrick Rinke^{1,2,3*}

¹Department of Applied Physics, Aalto University, P.O. Box 11000 ,
AALTO, FI-00076, Finland.

²Department of Physics, Technical University of Munich,
James-Franck-Strasse 1, Garching, 85748, Germany.

³Atomistic Modeling Center, Munich Data Science Institute, Technical
University of Munich, Walther-Von-Dyck Str. 10, Garching, 85748,
Germany.

⁴Munich Center for Machine Learning (MCML).

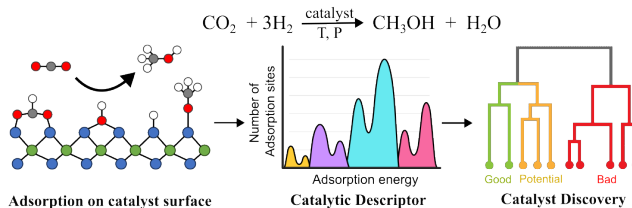
*Corresponding author(s). E-mail(s): patrick.rinke@aalto.fi;

Contributing authors: prajwal.pisal@aalto.fi; ondrej.krejci@aalto.fi;

[†]These authors contributed equally to this work.

Abstract

Transforming CO₂ into methanol represents a crucial step towards closing the carbon cycle, with thermoreduction technology nearing industrial application. However, obtaining high methanol yields and ensuring the stability of heterocatalysts remain significant challenges. Herein, we present a sophisticated computational framework to accelerate the discovery of novel thermal heterogeneous catalysts, using machine-learned force fields. We propose a new catalytic descriptor, termed adsorption energy distribution, that aggregates the binding energies for different catalyst facets, binding sites, and adsorbates. The descriptor is versatile and can easily be adjusted to a specific reaction through careful choice of the key-step reactants and reaction intermediates. By applying unsupervised machine learning and statistical analysis to a dataset comprising nearly 160 metallic alloys, we offer a powerful tool for catalyst discovery. Finally, we propose new promising candidate materials such as ZnRh and ZnPt₃, which to our knowledge, have not yet been tested, and discuss their possible advantage in terms of stability.



Keywords: CO₂ reduction, catalyst discovery, machine learning, adsorption energy

1 Introduction

Utilizing CO₂ in the production of useful chemicals closes the carbon loop and subsequently reduces CO₂ emissions. Converting CO₂ into liquid fuels or chemical feedstocks like methanol can decrease our dependence on fossil fuels [1]. The hydrogenation of CO₂ to methanol involves the reaction of two gases, similar to other important chemical processes like the Haber-Bosch synthesis [2], which produces ammonia, a precursor for fertilizers, from hydrogen and nitrogen. Both processes occur in thermochemical reactors and face significant energetic barriers, requiring high temperatures and pressures to yield the desired products. Heterogeneous catalysis is a key method to lower these reaction barriers, making the processes both technologically and economically viable [2, 3]. However, the economic feasibility of methanol synthesis has not yet been achieved [4].

The identification of an ideal CO₂ conversion method focuses primarily on two technological pathways: thermochemical [5] and electrochemical [6]. The thermochemical approach offers significant potential for rapid industrial adoption due to its resemblance to syngas conversion [5]. Current catalysts, typically based on the industrial syngas catalyst Cu/ZnO/Al₂O₃, suffer from low conversion rates, low selectivity [7], and oxidation poisoning [8]. Addressing these issues with better catalysts could increase performance and reduce costs [4]. However, experimentally screening materials to discover effective catalysts remains challenging due to the slow and expensive nature of catalyst testing and the vastness of the materials space.

Computational methods such as density functional theory (DFT) could provide a complementary, efficient and cost-effective alternative for catalyst discovery. However, calculating turn-over frequencies based on reaction barriers is often computationally intensive because it requires explicit transition state calculations. Moreover, many other factors like catalyst microstructure, reactor designs, mass and heat flows, etc. affect catalytic performance and necessitate multi-scale modeling [9, 10]. Consequently, approximate methods and concepts, such as the Sabatier principle that relate catalytic activity to the adsorption energies of reaction intermediates calculated using DFT [11], have been frequently employed in extensive searches for candidate materials [11–13]. Over the years, numerous approximations have been developed that have guided catalyst search, extending the Sabatier principle to correlate activity with more easily

obtainable activity descriptors, such as d -band center and scaling relations [12, 14, 15]. While these descriptors have provided valuable insight, their usefulness is often constrained to certain surface facets of material or a limited number of material families, such as d -metals.

Machine learning (ML) has recently emerged as a powerful alternative in materials research and is gaining traction, with several disciplines employing these techniques to expedite the discovery of new materials [13, 16–23]. Data-driven algorithms can analyze vast datasets of catalyst properties and performance, identifying complex relationships that may be beyond the reach of traditional descriptors [24, 25]. In the realm of heterogeneous catalysis, the ML methods can primarily be divided into two categories: mapping catalyst activity using new approximate descriptors [18, 20, 22] and prediction of adsorption energies using machine-learned force fields (MLFF) [17, 21]. These MLFFs, trained on extensive datasets of DFT calculations, offer a significant speedup (a factor of 10^4 or more) compared to DFT calculations while maintaining accuracy [26, 27]. Modern Sabatier principle-based approaches utilize MLFFs or specialized models to find (global) minimum adsorption energies across multiple material facets [13, 21]. Although several studies emphasize the importance of various catalyst facets [9, 28], these approaches predominantly utilize data from individual facets for material characterization. Consequently, the challenge persists: how can we effectively predict catalytic performance without limiting our scope to specific material families or facet orientations?

The absence of an adequate descriptor for the activity of complex materials motivates our exploration of methods to better represent contemporary industrial catalysts. These catalysts, composed of nanostructures with diverse surface facets and adsorption sites, present significant challenges in understanding their performance. This work seeks to address these challenges by focusing on three critical objectives: (1) developing a novel descriptor that captures the structural and energetic complexity of catalysts, (2) establishing an efficient workflow for large-scale computational screening, and (3) devising a robust framework to identify promising candidates from the resulting data.

Firstly, we seek to define a descriptor that encapsulates the inherent complexity of heterocatalytic materials. In this study, we introduce adsorption energy distributions (AEDs) as a tool to represent the spectrum of adsorption energies across various facets and binding sites of nanoparticle catalysts. Building on recent advances in characterizing structurally complex materials, such as high-entropy alloys [29, 30], we explore the potential of AEDs to fingerprint the material catalytic properties, using the CO_2 to methanol conversion reaction as a case study.

Secondly, we aim to establish a high-throughput and ML-enhanced workflow to accelerate the screening of catalytic materials using our newly formulated descriptor. Traditional density functional theory (DFT) approaches are computationally prohibitive for large-scale studies. To overcome this limitation, we leverage machine-learned force fields (MLFFs) from the Open Catalyst Project (OCP) [31, 32], enabling the rapid and accurate computation of adsorption energies. Our workflow generates an extensive dataset of AEDs, capturing over 877,000 adsorption energies for nearly 160 materials relevant to the CO_2 to methanol conversion reaction. To target the enhanced

reliability of our prediction and the effective use of ML models in catalyst discovery, we design a robust validation protocol.

Finally, we address the objective of developing a method to compare AED descriptors, which encode the energy landscape of materials, to those of known effective catalysts. This involves employing unsupervised learning techniques to analyze the extensive dataset of AEDs generated in this study. By treating AEDs as probability distributions, we quantify their similarity using the Wasserstein distance metric [33] and perform hierarchical clustering to group catalysts with similar AED profiles. This approach enables us to systematically compare the AEDs of new materials to those of established catalysts, identifying potential similarities that suggest comparable performance. Through this comparison with known effective catalysts, we seek to identify new materials with similar AEDs, highlighting a few promising candidates for further investigation.

2 Results and Discussion

In order to discover potential new catalysts for converting CO₂ into methanol, we present the workflow depicted in Fig. 1. The key steps are summarized here, with detailed implementation procedures and configurations available in the Methods section 3.

Search Space Selection:

To effectively reduce the search space for potential catalyst materials for CO₂ thermal conversion, we first isolated the metallic elements that have undergone prior experimentation for this process, as documented by Bahri *et al.* [34]. To maintain the prediction accuracy these elements also had to be part of the Open Catalyst 2020 (OC20) database [31]. The elements shortlisted are the following: K, V, Mn, Fe, Co, Ni, Cu, Zn, Ga, Y, Ru, Rh, Pd, Ag, In, Ir, Pt, and Au. We then proceeded to search through the Materials Project database [35] for stable and experimentally observed crystal structures associated with these metals and their bimetallic alloys. We compiled 216 stable phase forms involving both single metals and bimetallic alloys corresponding to our set of 18 elements. A detailed listing of these materials is provided in Tables S1 and S2 of the Supplementary Information. We performed bulk DFT optimization at the RPBE [36] level to align with the OC20 for the obtained materials. Optimization of 22 materials was not successful, and therefore, they were excluded from the materials list, as detailed in Table S2 in the Supplementary Information 3.5.

To identify the most crucial adsorbates for AEDs calculations, we perused the existing literature. An experimental investigation by Amman *et al.* [28] highlighted the presence of surface-bound radicals such as *H, *OH, *OCHO, and *OCH₃ as essential reaction intermediates in the thermocatalytic reduction of CO₂ to methanol. Based on these findings, we selected them for our AEDs calculations. With the help of `fairchem` repository tools by OCP [37], we created surfaces with their Miller index $\in \{-2, -1, \dots, 2\}$ and calculated their total energy using OCP MLFF. If we encountered multiple cuts for the same facet, we selected the one with lowest energy for further calculations. Then we engineered surface-adsorbate configurations for the most stable

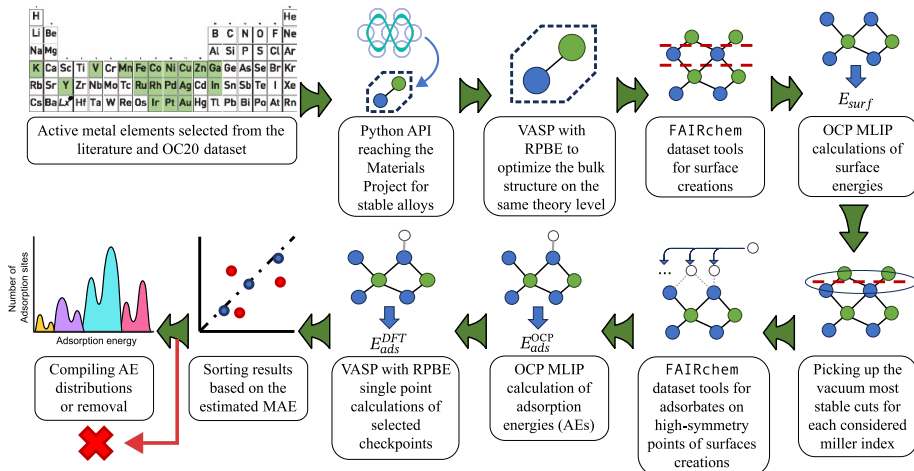


Fig. 1 Schematics of the workflow for adsorption energy distributions (AEDs) generation: The AED catalyst database was created through a series of steps, including the choice of metals, bulk optimization, selection of relevant surface geometries, preparation of adsorbate geometries, validation and compilation of AEDs as elaborated in the figure.

surface terminations across all facets within our defined Miller index range for the materials, as described in section 3.2, and optimized these configurations using the OCP MLFF. During this process, we discovered that six materials exhibited so large surface-adsorbate supercells, that their calculations were infeasible on available GPU resources, even with the effective OCP MLFF. Consequently, they were excluded from our study.

Validation and Data Cleaning:

In our work, we have employed the OCP `equiformer_v2` MLFF. Its reported accuracy for the adsorption energy of small molecular fragments is 0.23 eV [38]. However, `*OCHO` was not included in the OC20 database used for training the `equiformer_v2`, raising concerns about the accuracy of our adsorption energy predictions in this work. To benchmark `equiformer_v2` for our use case, we chose Pt, Zn, and NiZn and performed explicit DFT calculations (see Methods section for details). The comparison between predicted and DFT calculated adsorption energies can be found in Figure 2 and Table 1: The predictions for Pt are precise, whereas the NiZn results show some outliers, and there is a noticeable degree of scatter for Zn. Despite this, the overall mean absolute error (MAE) for the adsorption energies of the selected materials is 0.16 eV, which is quite impressive and falls within the reported accuracy for the employed MLFF.

To affirm the reliability of our predicted AEDs across a broader range of materials along with maintaining computational practicality, we integrated a validation step within our analysis workflow. We sampled the minimum, maximum, and median adsorption energies for each adsorbate-material pair from the predicted AEDs. We

Table 1 Mean absolute error (MAE) obtained through single-point comparison with DFT calculations for three selected materials – Pt, Zn and NiZn alloy. The MAE is compared to the estimated MAE (EMAE), which is obtained from single-point DFT calculations for only three selected structures per adsorbate-material combination.

Material: Adsorbate	Pt *H	*OH	*OCHO	*OCH ₃	Overall
MAE (eV)	0.02	0.05	0.06	0.09	0.06
EMAE (eV)	0.02	0.07	0.04	0.10	0.06
MAE/EMAE	0.97	0.66	1.59	0.93	0.96
Material: Adsorbate	Zn *H	*OH	*OCHO	*OCH ₃	Overall
MAE (eV)	0.10	0.13	0.10	0.15	0.12
EMAE (eV)	0.06	0.10	0.06	0.08	0.07
MAE/EMAE	1.68	1.34	1.68	1.95	1.64
Material: Adsorbate	NiZn *H	*OH	*OCHO	*OCH ₃	Overall
MAE (eV)	0.02	0.07	0.09	0.06	0.06
EMAE (eV)	0.02	0.05	0.09	0.02	0.05
MAE/EMAE	0.73	1.36	1.04	2.61	1.27

performed single-point DFT calculations on these selected systems and compared with the adsorption energy predictions of the OCP MLFF. The difference is compiled in an ‘estimated MAE’ (EMAE). Comparisons between EMAE and the all-encompassing MAE for our complete test set are presented in Table 1. While the EMAE may differ from the actual MAE by up to a factor of three for specific adsorbates, it generally remains in close proximity to the actual MAE, thus serving as a reliable gauge of data quality.

The validation step is connected with the final data-cleaning when we exclude any material with an EMAE surpassing the threshold of 0.25 eV. Consequently, 29 materials were expunged from our dataset, retaining 159 materials. Most materials flagged for significant EMAEs exhibited magnetic properties, exemplified by materials like MnCo, MnGa, or FeCo. Magnetism presents significant challenges for the non-spin-polarized DFT calculations used in OC20 and in this work. A complete list of estimated MAEs for the remaining 159 materials is accessible in [39].

Adsorption Energy Distributions:

Lastly, to compile the AEDs, we examined the relaxed configurations. For many distinct initial configurations of identical adsorbates, materials, and facets that converged to the same final structure, only one of them is considered in the AED. In our final compilation, we transformed all AEDs into histograms that depict the probability distribution of adsorption sites falling within 0.1 eV energy intervals. Each AED was normalized, ensuring that the aggregate probability of adsorption sites per adsorbate and material equaled one. This standardization facilitates direct comparisons across materials with different numbers of adsorption sites, which can range from several tens

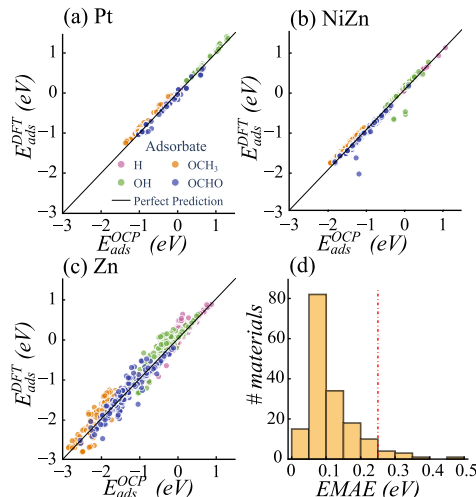


Fig. 2 Validation of results:(a-c) The comparison of adsorption energy predicted by the OCP equiformer_v2 MLFF against single-point DFT calculations, for (a) Pt, (b) Zn and (c) NiZn. (d) Histogram of EMAEs for the materials that has been calculated with the OCP MLFF, with the 0.25 eV cut-off line, showing that majority of the materials has their EMEA between 0.05 – 0.10 eV. Out of a total of 188 OCP calculated materials, 17 are not shown here as their EMAE is above 0.5 eV.

to nearly 10,000 for a single material, depending upon the complexity and symmetry of its bulk structure. For illustrative purposes, Fig. 3 displays examples of AEDs for selected materials. The AEDs for all investigated materials is shown in Fig. S1 in the Supplementary Information 3.5.

Inspection of Fig. 3 and Fig S1 reveals that adsorption energies span a wide interval from -7.42 eV to 2.40 eV. We included energies above zero, although positive adsorption energies are typically indicative of molecular desorption. However, the adsorption energies reported in this work do not include entropy and pressure terms, which could shift the energies to more negative values. Secondly, the adsorption energy of radicals is somewhat ill-defined, if different desorption channels are conceivable. Since our objective is to achieve a qualitative comparison across materials, the price energy zero is of no relevance, as long as it is chosen consistently.

The AEDs exhibit varying dispersion and forms, indicating fluctuations in adsorption energy and related activity levels across the material space. The adsorption energies of *OCH₃ (E_{ads}) are generally the lowest, followed by those of *OCHO, which are approximately 0.5–1 eV higher. However, certain materials, such as K (illustrated in Fig. 3(b)), show unique distribution overlaps for *OCHO and *OCH₃. Meanwhile, *H and *OH have comparatively higher E_{ads} values, although their order is inconsistent. For instance, in some cases, *H has the highest E_{ads} , particularly for K and Y₃In₅, whereas the opposite trend is observed for other materials like Ni. Single metal distributions are generally narrower and higher, as seen in the examples of K and Ni. Similarly, alloys composed of elements with high symmetry, such as CuZn, also exhibit narrow AEDs.

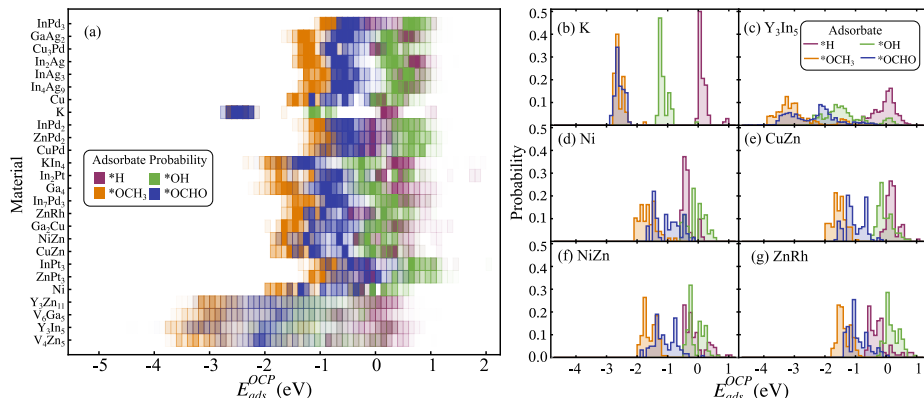


Fig. 3 AEDs for selected subset of materials: (a) AEDs for 26 materials with the amplitude of the distribution encoded in the intensity of the corresponding color; detailed AEDs for (b) K, (c) Y₃In₅, (d) Ni, (e) CuZn, (f) NiZn, (g) ZnRh.

If the AEDs of a material predominantly align around the adsorption energy linked to maximal activity according to the Sabatier principle, the material is a strong candidate for a good catalyst. Conversely, complex alloys with low symmetry, such as Y₃In₅ (shown in the lower section of Fig. 3(a) and in Fig. 3(c)), display broad AED spreads. Extremely low adsorption energies can lead to catalyst poisoning, while excessively high energies can significantly reduce catalytic activity. Therefore, broad distributions are less desirable, as only a small portion of the material’s surface contributes effectively to catalytic processes.

Unsupervised Learning: Catalyst Discovery

Although the ideal AEDs for the four adsorbates remain unknown, it is feasible to approximate their reactivity using AEDs based on their resemblance to previously identified, efficacious catalytic materials. In this context, our AEDs can be conceptualized as four-dimensional probability distributions. To quantify similarities across AEDs of different materials, we employ the Wasserstein distance as the metric [33]. By computing Wasserstein distances for all possible material combinations, we construct a distance matrix. To interpret the distance matrix, we apply hierarchical agglomerative clustering with Ward’s linkage [40], which facilitates the identification of materials with similar AEDs. The outcomes of this clustering analysis are depicted in Fig. 4.

For a clustering threshold corresponding to a Wasserstein distance of 0.025, we arrive at a total of 19 distinct clusters, with potassium (K) forming its own, isolated, unnumbered cluster. The separation between clusters 11 to 19 and clusters 1 to 10 is considerable. The distinguishing feature is the broadness of the AEDs. The distributions in clusters 11 to 19 are noticeably broader than in clusters 1 to 10. Representative examples are depicted in Fig. 3(a). The four materials at the bottom of the figure (Y₃Zn₁₁, V₆Ga₅, Y₃In₅, V₄Zn₅) pertain to cluster 18, whereas the rest belong to clusters 8 to 10. Further details are available in Fig. S1 of the Supplementary Information, presenting the clustering of all considered materials. AEDs exhibit variability across

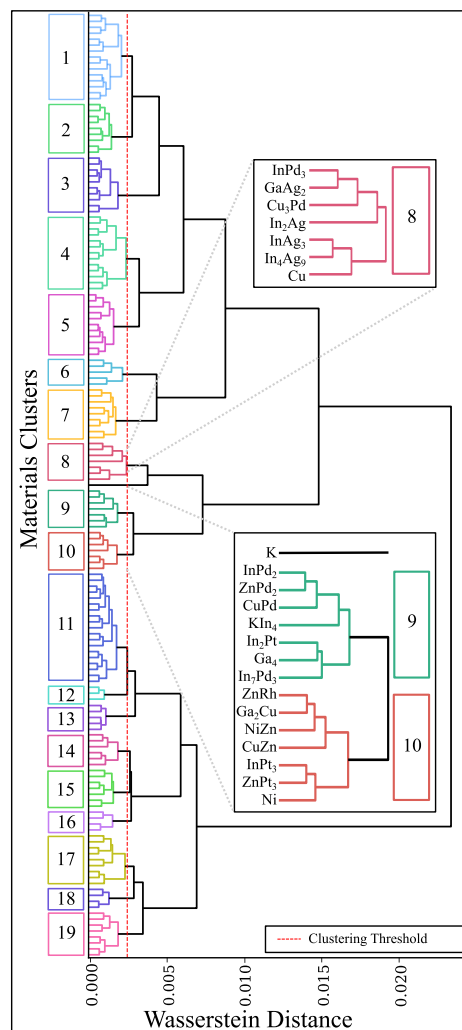


Fig. 4 Hierarchical clustering of the materials, based on the Wasserstein Distances: The graph show that all 159 materials were assembled into 19 clusters, based on the similarity between of the AEDs, with the exception of potassium, which is dissimilar to nearby materials and forms a single material, non-numbered cluster. This can be seen in detail in the insets, where also materials in clusters 8, 9 and 10 are can be seen. The cluster 10 contains several alloys, which are part of known high-yield catalysts as well as new potentially active materials.

distinct clusters (1 – 10) but show remarkable similarity within each individual cluster. For example, the AEDs for Ni, CuZn, NiZn, and ZnRh illustrated in Fig. 3(d-g) belong to the same cluster.

Clusters 8 through 10 aggregate into a larger cluster with relatively homogeneous AEDs, encompassing materials such as Cu, a notably active component within known Cu/ZnO/Al₂O₃ catalysts [28, 34]. The clusters also contain non-Cu materials such as Zn-Pd, Pd-In, Pt-In, and Ni-Zn in different compositions that have been reported as catalytic converters of CO₂ to methanol [34, 41]. Several bimetallic alloys are grouped with these materials that have not been tested for CO₂ to methanol conversion, up to our knowledge: Ga-Ag, In-Ag, K-In, Zn-Rh, and Zn-Pt, which also occur in various compositions. While most of these materials have either shown good catalytic performance or some have not been tested, potassium (K) (the lone non-numbered cluster), as a pure metal, is likely to undergo rapid oxidation under reaction conditions. Therefore, we anticipate that this particularly large cluster, consisting of clusters 8-10, is likely too diverse to pinpoint only catalytically active materials.

Upon closer inspection, ZnRh and ZnPt₃ stand out as new candidates. They are part of cluster 10, which also includes Ga₂Cu, NiZn, InPt₃, Ni and mainly CuZn, but have not been tested for CO₂ to methanol conversion. It is evident that Zn incorporation into Cu enhances the activity of Cu-based catalysts, predominantly due to the formation of a Cu-Zn alloy [28, 42, 43]. NiZn has also been identified as an effective CO₂ catalyst [41]. Catalysts such as Cu/Ga₂O₃ and Pt/In₂O₃, known for their high methanol yield, likely include Ga₂Cu and InPt₃ alloys, respectively. Finally, Ni is often part of catalysts for CO₂ transformation to methane [44, 45]. The strong catalytic activity of Ga₂Cu, NiZn, InPt₃, Ni and mainly CuZn in this cluster suggest that also ZnRh and ZnPt₃ should have a high activity.

Statistical Analysis and Discussion:

AEDs could serve as a descriptor of activity, however, the vast number of parameters (at least 388 bins in the distribution) makes it challenging to analyze them manually. To further our insight into the generated data, we conducted a statistical analysis of our AEDs (SAAEDs) that facilitates comparison with previous adsorption energy-based studies. An example can be seen in Table 2, where we present the minimum adsorption energies for a subset of materials featured in Fig 3(a).

Our SAAED analysis revisits individual binding energies and connects to the Sabatier principle. For instance, the results for *OH, *OCHO, and *OCH₃ can be compared to the volcano plot in Studt *et al.* [43], that relates the catalytic activity of the studied materials to the oxygen adsorption energy. In line with our approach, their work compares potential catalyst materials to Cu, although their focus lies on single-facet surfaces. Following previous findings that the Cu(211) facet is more active than the close-packed Cu(111) surface [42], Studt *et al.* use Cu(211) as their reference. The catalytic activity of Cu is further enhanced when Zn is added to the Cu(211) surface (referred to as Cu+Zn in the article). The oxygen adsorption energy decreases upon Zn addition, which indicates that the optimal oxygen adsorption energy should be lower than its minimal adsorption energy on the Cu(211) surface. Our data is consistent with those findings for the majority of our promising candidate materials. The minimal adsorption energy (E_{ads}^{min}) for all the oxygen-containing adsorbates on the majority of the materials in cluster 10 (highlighted in Table 2), including ZnRh, lies below that of

Table 2 Extract of the statistical analysis on the AEDs: The minimum of the OCP MLFF predicted adsorption energies $E_{\text{ads}}^{\text{min}}$ which is basically comparable to the adsorption energy used in Sabatier principle. We show the predicted $E_{\text{ads}}^{\text{min}}$ for the same materials as in Fig. 3 (i.e. clusters 8 – 10 and 18), for all the considered adsorbates. The materials of cluster 10 are highlighted in bold.

Material	*H $E_{\text{ads}}^{\text{min}}$	*OH $E_{\text{ads}}^{\text{min}}$	*OCH ₃ $E_{\text{ads}}^{\text{min}}$	*OCHO $E_{\text{ads}}^{\text{min}}$
InPd ₃	-0.54	0.27	-1.04	-1.22
GaAg ₂	0.22	-0.25	-1.06	-1.80
Cu ₃ Pd	-0.17	-0.04	-1.05	-1.53
In ₂ Ag	0.27	-0.06	-0.96	-1.59
InAg ₃	0.24	0.09	-0.88	-1.41
In ₄ Ag ₉	0.12	-0.07	-0.93	-1.53
Cu	-0.14	-0.18	-1.29	-1.64
K	-0.01	-1.31	-2.81	-2.77
InPd ₂	-0.39	-0.04	-1.09	-1.57
ZnPd ₂	-0.38	0.06	-1.11	-1.44
CuPd	-0.44	0.03	-1.12	-1.41
KIn ₄	-0.40	-1.11	-2.36	-2.46
In ₂ Pt	-0.33	-0.54	-1.69	-2.12
Ga ₄	-0.71	-0.98	-1.73	-2.36
In ₇ Pd ₃	-0.36	-0.33	-1.20	-1.80
ZnRh	-0.63	-0.30	-1.39	-1.71
Ga₂Cu	-0.20	-0.92	-1.36	-2.06
NiZn	-0.49	-0.49	-1.81	-1.93
CuZn	-0.19	-0.44	-1.67	-1.94
InPt₃	-0.59	0.13	-1.09	-1.41
ZnPt₃	-0.43	0.10	-0.98	-1.40
Ni	-0.53	-0.54	-1.66	-2.05
Y ₃ Zn ₁₁	-0.89	-2.22	-3.92	-3.68
V ₆ Ga ₅	-1.30	-3.37	-5.44	-3.78
Y ₃ In ₅	-0.88	-2.51	-4.61	-3.93
V ₄ Zn ₅	-1.13	-2.29	-3.72	-3.87

Cu (our Cu data also covers the (211) surface) and is closely aligned across the materials. The exceptions are InPt₃ and ZnPt₃, in which the minima lie slightly above those of Cu, while both materials exhibit similar $E_{\text{ads}}^{\text{min}}$ for all other adsorbates. This difference suggests that InPt₃ and ZnPt₃ may feature slightly different CO₂ conversion mechanisms.

Using minimum adsorption energies derived from ML models is comparable to previously studied methods for identifying global minima [13, 21]. Although the techniques by Lan *et al.* [21] and Chen *et al.* [13] might be more appropriate for the straightforward application of the Sabatier principle, our approach excels in providing more comprehensive information on various facets of catalytic materials. We have compiled this information for selected materials in Table S1 in the Supplementary Information. For example, the AED spread across energies, which can be deduced from the standard deviation $E_{\text{ads}}^{\text{std}}$, provides information about the percentage of the surface area usable for catalytic conversion.

Ultimately, both AEDs and SAAEDs, available on Zenodo [39], can serve as material fingerprints. The SAAED acts like a materials descriptor, similar to the Magpie

descriptor [16], but can be adapted to specific reactions through the choice of adsorbates, offering more detailed and relevant material information. Optionally, specific descriptors (AED, SAAED) and general descriptors (like Magpie [16]) may be combined to enhance the information that might be lacking in ML models from theoretical calculations.

Both catalyst descriptors are tailored for an extensive search for catalytically active material candidates, yet they omit the effect of support, additives, and preparation procedures that can change the size of the active material nanoparticles and the area of different facets. Moreover, our AED descriptor does not take the facet area into account, and is therefore insensitive to morphology changes of the catalysts under reaction conditions.

To finalize the analysis of our results, the similarity of the SAAED and Wasserstein distances of ZnRh and ZnPt₃ to good catalysts in the literature suggests that they could be good catalyst candidates. As Cu-based catalysts are known for their vulnerability to degradation [5], it is therefore reasonable to pre-examine these materials also in terms of stability. Given the harsh reaction conditions, mainly temperatures around 800 K [34], the melting temperature of the catalyst is directly related to the stability of the catalyst. The melting temperature of both ZnRh and ZnPt₃ is higher than that of pure copper or CuZn [35], suggesting that our new candidates could also be more durable.

Summary:

In summary, we have established a fast and reliable computational approach for discovering new catalyst candidates for the conversion of CO₂ to methanol utilizing data-driven methodologies such as MLFFs and hierarchical clustering. Beginning with a list of potential metallic elements, we extracted experimentally verified materials from the Materials Project database. By integrating tools from `fairchem`, mainly OCP MLFFs, we created an extensive database of adsorption energies for a wide range of materials facets and possible adsorption sites. We compiled this information to obtain a novel material descriptor, AED, which offers a more effective representation of the complex nature of heterocatalysts compared to standard methods. By carefully choosing the adsorbates, the descriptor can be tailored to provide the most information for any heterocatalytic reaction under study. Through efficient sampling for validation, we were able to quantify the quality of our workflow with a minimal number of DFT calculations while ensuring the high quality of our database. We grouped the materials by their AED similarity using statistical methods and clustering. This allowed us to pinpoint promising new candidates, namely ZnRh and ZnPt₃, based on their resemblance to known effective catalysts. Our results indicate that AEDs, together with statistical analysis, can serve as material fingerprints, aiding in the prediction of catalyst activity and accelerating the discovery process.

3 Methods

3.1 Bulk Preparation

We sourced the bulk geometries of experimentally observed metals and alloys of select elements from the Materials Project Database [35]. These structures were selected on the basis of their stability, as indicated by cohesive energies located on the convex hull. We optimized the bulk geometries using the RPBE functional [36] as implemented in the Vienna ab-initio Simulation Package (VASP) [46, 47]. A plane-wave cutoff of 500 eV was used in the first attempt to relax the structures. If the initial run did not converge, we increased the cut-off to 550 eV. We sampled the Brillouin zone with a k -point spacing of 0.17 \AA^{-1} . The calculations were automated using the workflows developed by Atomate [48] based on the Pymatgen [49], Custodian [50] and Fireworks [51] libraries.

3.2 Surface Generation and Selection

We generated all symmetrically distinct surfaces of Miller indices $\in \{-2, -1, 0, \dots, 2\}$ from the relaxed bulk structures using the workflow implemented by OCP, i.e. `fairchem` [31, 37]. We fixed the thickness of the slabs to 7 \AA with a vacuum of 20 \AA along the z -direction. These parameters were chosen to be consistent with the OC20 dataset that was used to train the OCP MLFFs to maintain high prediction accuracy [31]. With the pre-trained `gemnet-oc` MLFF [52], we relaxed the surfaces and obtain their *total energy*. When encountering different surface terminations for a given facet, i.e., different absolute positions of the surface plane, we retained only the structure with the lowest energy.

3.3 Generation and Relaxation of Adsorbate-Surface Configurations

The selected surfaces were used to generate adsorbate-surface configurations using neutral fragments of `*H`, `*OH`, `*OCHO` and `*OCH3` by means of the `fairchem` input generation workflow [37]. The systems were relaxed using an *adsorption energy*-based OCP `equiformer_v2` MLFF to obtain the relaxed geometries. The corresponding adsorption energy E_{ads} follows the OCP convention $E_{ads} = E_{system} - E_{surface} - E_{adsorbate}$, where $E_{adsorbate}$ is composed of atomic energies, defined in the work of Chanussot *et. al.* [31]. Here, $E_{adsorbate}$ is -3.477 eV for `*H`, -10.552 eV for `*OH`, -24.917 eV for `*OCH3` and -25.161 eV for `*OCHO`. The force convergence criterion for the adsorbate relaxations was set to 0.03 eV/\AA .

The `equiformer_v2` relaxations were performed using NVIDIA Ampere A100 GPUs, completing each relaxation in just a few seconds, whereas corresponding DFT calculations would require several hours on two AMD Rome 7H12 CPUs with 64 cores each. Relaxed configurations of the same material and facet were compared to identify redundancies. If two or more configurations exhibited identical adsorbate geometries (and thus energies) within a tolerance of 0.1 \AA in each spatial direction, only one configuration was retained for further consideration. Nonunique configurations and their corresponding adsorption energies were excluded. With this we ensured that

the remaining data represents meaningful adsorption positions and thus capture the material’s true energetic landscape.

We aggregated the adsorption energies into AEDs for every adsorbate and material. The AED is represented by a histogram of 0.1 eV wide bins, that are centered along energies $\{-7.4, -7.3, \dots, 2.4\}$. The histogram settings were chosen so that each AED has at least five empty bins on either side, which is important for further analysis. We normalized the AEDs by dividing the entry in each bin by the number of unique adsorption configurations.

3.4 Estimation of the Mean Absolute Error for the Adsorption Energy Prediction

We initially evaluated the performance of the `equiformer_v2` model on Pt, Zn, and NiZn. For this evaluation, we used the adsorbate-surface geometries relaxed with `equiformer_v2` and the clean surface geometries optimized using `gemnet-oc`. We then computed the DFT adsorption energies without further relaxations. We used the same `VASP` settings as for the generation of the OC20 dataset [31], but increased the plane-wave cutoff to 450 eV. This adjustment was made on the basis of our preliminary estimate for selected materials to ensure high accuracy of both predicted and calculated adsorption energies. The resulting adsorption energies are shown in Figure 2.

To determine the EMAE, we employed a computationally efficient strategy to validate the predictions of the OCP MLFF model. From the AED of a given material-adsorbate pair, we chose the three configurations that correspond to the mean, median, and maximum adsorption energy. Subsequently, we carried out single-point DFT calculations for the corresponding adsorbate-surface systems and clean surfaces to compute the adsorption energies.

The EMAE was determined as the average of the three absolute errors. As discussed in Section 2, materials with EMAEs exceeding 0.25 eV were excluded from further analysis due to their insufficient accuracy.

3.5 Unsupervised Learning

We concatenated the four AEDs for each material into a single distribution, where the added buffer (see Section 3.3) ensures no possible overlap between distributions. We then computed Wasserstein distances for all pairs of materials to create a single distance matrix. Given two 1D probability mass functions, μ and ν , the first Wasserstein distance between the distributions is defined as [53]:

$$W_1(\mu, \nu) = \inf_{\gamma \in \Gamma(\mu, \nu)} \int_{\mathbb{R} \times \mathbb{R}} \|x - y\| d\gamma(x, y) \quad (1)$$

where $\Gamma(\mu, \nu)$ is the set of (probability) distributions on $\mathbb{R} \times \mathbb{R}$ whose marginals are μ and ν on the first and second factors, respectively. For a given value x , $\mu(x)$ gives the probability of μ at position x , and the same for $\nu(x)$.

Using these Wasserstein distances, we performed agglomerative hierarchical clustering with Ward linkage [40, 54, 55]. We utilized the Python-based SciPy library [53]

to compute the distances and to perform the clustering on the distance matrix. We used a clustering threshold of 0.0025 to define the maximum distance at which clusters are merged.

Supplementary information. The Supplementary information contains: Table S1 – All 159 materials used in final evaluation; Table S2 – All materials removed from the final evaluation; Figure S1 – Adsorption energy distributions and hierarchical clustering of all 159 materials; Table S3 – Statistical analysis on the AEDs for a subset of materials shown in Fig. 3.

Acknowledgements. The authors would like to thank Annukka Santasalo-Aarnio and Arpad Toldy for fruitful discussions. O.K. and P.P. express their gratitude to Kirby Broderick, Adeesh Koluru, Brook Wander, John Kitchin and other Kitchin research group members at Carnegie Mellon University and Zachary Ulissi at Meta, for their help with the OCP models. This project received funding from the European Union – NextGenerationEU instrument and the Research Council of Finland’s AICoN project (grant number no. 348179). The authors gratefully acknowledge CSC – IT Center for Science, Finland, and the Aalto Science-IT project for the generous computational resources.

Declarations

The authors declare no conflicts of interest. The data published in this study can be found in [39]. P.P. and O.K. created the workflow and proceeded the calculation. P.R. supervised the work. All authors contributed to the manuscript.

Editorial Policies for:

Springer journals and proceedings: <https://www.springer.com/gp/editorial-policies>

Nature Portfolio journals: <https://www.nature.com/nature-research/editorial-policies>

Scientific Reports: <https://www.nature.com/srep/journal-policies/editorial-policies>

BMC journals: <https://www.biomedcentral.com/getpublished/editorial-policies>

References

- [1] Ye, R.-P., Ding, J., Gong, W., Argyle, M.D., Zhong, Q., Wang, Y., Russell, C.K., Xu, Z., Russell, A.G., Li, Q., Fan, M., Yao, Y.-G.: CO₂ hydrogenation to high-value products via heterogeneous catalysis. *Nature Communications* **10**(5698) (2019)
- [2] Rohr, B.A., Singh, A.R., Nørskov, J.K.: A theoretical explanation of the effect of oxygen poisoning on industrial haber-bosch catalysts. *Journal of Catalysis* **372**, 33–38 (2019) <https://doi.org/10.1016/j.jcat.2019.01.042>

- [3] Saito, M., Fujitani, T., Takeuchi, M., Watanabe, T.: Development of copperzinc oxide-based multicomponent catalysts for methanol synthesis from carbon dioxide and hydrogen. *Applied Catalysis A: General* **138**(2), 311–318 (1996)
- [4] Nyári, J., Magdeldin, M., Larmi, M., Järvinen, M., Santasalo-Aarnio, A.: Techno-economic barriers of an industrial-scale methanol CCU-plant. *Journal of CO₂ Utilization* **39**, 101166 (2020) <https://doi.org/10.1016/j.jcou.2020.101166>
- [5] Ganesh, I.: Conversion of carbon dioxide into methanol – a potential liquid fuel: Fundamental challenges and opportunities (a review). *Renewable and Sustainable Energy Reviews* **31**, 221–257 (2014) <https://doi.org/10.1016/j.rser.2013.11.045>
- [6] Tran, K., Ulissi, Z.W.: Active learning across intermetallics to guide discovery of electrocatalysts for CO₂ reduction and H₂ evolution. *Nature Catalysis* **1**, 696–703 (2018) <https://doi.org/10.1038/s41929-018-0142-1>
- [7] Wang, L., Etim, U.J., Zhang, C., Amirav, L., Zhong, Z.: CO₂ activation and hydrogenation on Cu-ZnO/Al₂O₃ nanorod catalysts: An in situ FTIR study. *Nanomaterials* **12**(15), 2527 (2022) <https://doi.org/10.3390/nano12152527>
- [8] Li, D., Wang, Z., Jin, S., Zhu, M.: Deactivation and regeneration of the commercial Cu/ZnO/Al₂O₃ catalyst in low-temperature methanol steam reforming. *Sci China Chem* **66**, 3645–3652 (2023) <https://doi.org/10.1007/s11426-023-1789-3>
- [9] Bruix, A., Margraf, J.T., Andersen, M., Reuter, K.: First-principles-based multiscale modelling of heterogeneous catalysis. *Nature Catalysis* **2**, 659–670 (2019) <https://doi.org/10.1038/s41929-019-0298-3>
- [10] Posada-Borbón, A., Grönbeck, H.: A first-principles-based microkinetic study of CO₂ reduction to CH₃OH over In₂O₃(110). *ACS Catal.* **11**(15), 9996–10006 (2021) <https://doi.org/10.1021/acscatal.1c01707>
- [11] Che, M.: Nobel prize in chemistry 1912 to Sabatier: Organic chemistry or catalysis? *Catalysis Today* **218–219**, 162–171 (2013) <https://doi.org/10.1016/j.cattod.2013.07.006> . Catalysis: From the active sites to the processes
- [12] Medford, A.J., Vojvodic, A., Hummelshøj, J.S., Voss, J., Abild-Pedersen, F., Studt, F., Bligaard, T., Nilsson, A., Nørskov, J.K.: From the Sabatier principle to a predictive theory of transition-metal heterogeneous catalysis. *Journal of Catalysis* **328**, 36–42 (2015) <https://doi.org/10.1016/j.jcat.2014.12.033>
- [13] Chen, Z.W., Li, J., Ou, P., Huang, J.E., Wen, Z., Chen, L., Yao, X., Cai, G., Yang, C.C., Singh, C.V., Jiang, Q.: Unusual Sabatier principle on high entropy alloy catalysts for hydrogen evolution reactions. *Nature Communications* **15**(1), 359 (2024) <https://doi.org/10.1038/s41467-023-44261-4>

- [14] Jones, G., Bligaard, T., Abild-Pedersen, F., Nørskov, J.K.: Using scaling relations to understand trends in the catalytic activity of transition metals. *Journal of Physics: Condensed Matter* **20**(6), 064239 (2008) <https://doi.org/10.1088/0953-8984/20/6/064239>
- [15] Vogt, C., Weckhuysen, B.M.: The concept of active site in heterogeneous catalysis. *Nature Reviews Chemistry* **6**(2), 89–111 (2022) <https://doi.org/10.1038/s41570-021-00340-y>
- [16] Ward, L., Agrawal, A., Choudhary, A., Wolverton, C.: A general-purpose machine learning framework for predicting properties of inorganic materials. *npj Computational Materials* **2**(1), 16028 (2016) <https://doi.org/10.1038/npjcompumats.2016.28>
- [17] Ulissi, Z.W., Tang, M.T., Xiao, J., Liu, X., Torelli, D.A., Karamad, M., Cummins, K., Hahn, C., Lewis, N.S., Jaramillo, T.F., Chan, K., Nørskov, J.K.: Machine-learning methods enable exhaustive searches for active bimetallic facets and reveal active site motifs for CO₂ reduction. *ACS Catalysis* **7**(10), 6600–6608 (2017) <https://doi.org/10.1021/acscatal.7b01648>
- [18] Andersen, M., Levchenko, S.V., Scheffler, M., Reuter, K.: Beyond scaling relations for the description of catalytic materials. *ACS Catalysis* **9**, 2752–2759 (2019) <https://doi.org/10.1021/acscatal.8b04478>
- [19] Himanen, L., Geurts, A., Foster, A.S., Rinke, P.: Data-driven materials science: Status, challenges, and perspectives. *Adv. Sci.* **6**(21), 1900808 (2019)
- [20] Zhang, N., Yang, B., Liu, K., Li, H., Chen, G., Qiu, X., Li, W., Hu, J., Fu, J., Jiang, Y., Liu, M., Ye, J.: Machine learning in screening high performance electrocatalysts for CO₂ reduction. *Small Methods* **5**(11), 2100987 (2021) <https://doi.org/10.1002/smt.202100987>
- [21] Lan, J., Palizhati, A., Shuaibi, M., *et al.*: AdsorbML: a leap in efficiency for adsorption energy calculations using generalizable machine learning potentials. *npj Comput Mater* **9**, 172 (2023) <https://doi.org/10.1038/s41524-023-01121-5>
- [22] Mou, L.-H., Han, T., Smith, P.E.S., Sharman, E., Jiang, J.: Machine learning descriptors for data-driven catalysis study. *Advanced Science* **10**(22), 2301020 (2023) <https://doi.org/10.1002/advs.202301020> <https://onlinelibrary.wiley.com/doi/pdf/10.1002/advs.202301020>
- [23] Zhang, Y., Ling, C.: A strategy to apply machine learning to small datasets in materials science. *npj Computational Materials* **4**(1), 25 (2018) <https://doi.org/10.1038/s41524-018-0081-z>
- [24] Mamun, O., Winther, K.T., Boes, J.R., Bligaard, T.: A bayesian framework for adsorption energy prediction on bimetallic alloy catalysts. *npj Computational*

Materials **6**(1), 177 (2020) <https://doi.org/10.1038/s41524-020-00447-8>

- [25] Fiedler, L., Modine, N.A., Schmerler, S., Vogel, D.J., Popoola, G.A., Thompson, A.P., Rajamanickam, S., Cangi, A.: Predicting electronic structures at any length scale with machine learning. *npj Computational Materials* **9**(1), 115 (2023) <https://doi.org/10.1038/s41524-023-01070-z>
- [26] Kang, P.-L., Shang, C., Liu, Z.-P.: Large-scale atomic simulation via machine learning potentials constructed by global potential energy surface exploration. *Accounts of Chemical Research* **53**(10), 2119–2129 (2020) <https://doi.org/10.1021/acs.accounts.0c00472>
- [27] Chen, D., Shang, C., Liu, Z.-P.: Machine-learning atomic simulation for heterogeneous catalysis. *npj Computational Materials* **9**(1), 2 (2023) <https://doi.org/10.1038/s41524-022-00959-5>
- [28] Amann, P., Klötzer, B., Degerman, D., Köpfle, N., Götsch, T., Lömker, P., Rameshan, C., Ploner, K., Bikaljevic, D., Wang, H.-Y., Soldemo, M., Shipilin, M., Goodwin, C.M., Gladh, J., Stenlid, J.H., Börner, M., Schlueter, C., Nilsson, A.: The state of zinc in methanol synthesis over a Zn/ZnO/Cu(211) model catalyst. *Science* **376**(6593), 603–608 (2022) <https://doi.org/10.1126/science.abj7747>
<https://www.science.org/doi/pdf/10.1126/science.abj7747>
- [29] Batchelor, T.A., Pedersen, J.K., Winther, S.H., Castelli, I.E., Jacobsen, K.W., Rossmeisl, J.: High-entropy alloys as a discovery platform for electrocatalysis. *Joule* **3**(3), 834–845 (2019)
- [30] Pedersen, J.K., Batchelor, T.A., Bagger, A., Rossmeisl, J.: High-entropy alloys as catalysts for the CO₂ and CO reduction reactions. *ACS catalysis* **10**(3), 2169–2176 (2020)
- [31] Chanussot, L., Das, A., Goyal, S., Lavril, T., Shuaibi, M., Riviere, M., Tran, K., Heras-Domingo, J., Ho, C., Hu, W., Palizhati, A., Sriram, A., Wood, B., Yoon, J., Parikh, D., Zitnick, C.L., Ulissi, Z.: Open Catalyst 2020 (OC20) dataset and community challenges. *ACS Catalysis* **11**(10), 6059–6072 (2021) <https://doi.org/10.1021/acscatal.0c04525>
- [32] Tran, R., Lan, J., Shuaibi, M., Wood, B.M., Goyal, S., Das, A., Heras-Domingo, J., Kolluru, A., Rizvi, A., Shoghi, N., Sriram, A., Therrien, F., Abed, J., Voznyy, O., Sargent, E.H., Ulissi, Z., Zitnick, C.L.: The Open Catalyst 2022 (OC22) dataset and challenges for oxide electrocatalysts. *ACS Catal.* **13**(5), 3066–3084 (2023) <https://doi.org/10.1021/acscatal.2c05426>
- [33] Ramdas, A., García Trillos, N., Cuturi, M.: On Wasserstein two-sample testing and related families of nonparametric tests. *Entropy* **19**(2), 47 (2017)

- [34] Bahri, S., Pathak, S., Singhahluwalia, A., Malav, P., Upadhyayula, S.: Meta-analysis approach for understanding the characteristics of CO₂ reduction catalysts for renewable fuel production. *Journal of Cleaner Production* **339**, 130653 (2022) <https://doi.org/10.1016/j.jclepro.2022.130653>
- [35] Jain, A., Ong, S.P., Hautier, G., Chen, W., Richards, W.D., Dacek, S., Cholia, S., Gunter, D., Skinner, D., Ceder, G., Persson, K.A.: Commentary: The Materials Project: A materials genome approach to accelerating materials innovation. *APL Materials* **1**(1), 011002 (2013) <https://doi.org/10.1063/1.4812323> https://pubs.aip.org/aip/apm/article-pdf/doi/10.1063/1.4812323/13163869/011002_1_online.pdf
- [36] Hammer, B., Hansen, L.B., Nørskov, J.K.: Improved adsorption energetics within density-functional theory using revised Perdew-Burke-Ernzerhof functionals. *Phys. Rev. B* **59**, 7413–7421 (1999) <https://doi.org/10.1103/PhysRevB.59.7413>
- [37] FAIR-Chem: fairchem: A FAIR-Chem Project Repository. GitHub (2024). <https://github.com/FAIR-Chem/fairchem>
- [38] Liao, Y.-L., Wood, B., Das, A., Smidt, T.: Equiformerv2: Improved equivariant transformer for scaling to higher-degree representations. arXiv preprint arXiv:2306.12059 (2023). Published as a conference paper at ICLR 2024
- [39] Pisal, P., Krejci, O.: Final Geometries and Energies, Statistical Analysis and Estimated Errors of Single Metals and Bimetallics for CO₂ to Methanol Conversion. <https://doi.org/10.5281/zenodo.13370374> . <https://doi.org/10.5281/zenodo.13370374>
- [40] Jr., J.H.W.: Hierarchical grouping to optimize an objective function. *Journal of the American Statistical Association* **58**(301), 236–244 (1963) <https://doi.org/10.1080/01621459.1963.10500845>
- [41] Dongapure, P., Tekawadia, J., Thundiyil, S., Caha, I., Deepak, F.L., Devi, R.N.: Mechanistic insights into near ambient pressure activity of intermetallic NiZn/TiO₂ catalyst for CO₂ conversion to methanol. *ChemCatChem* **15**(1), 202201150 (2023) <https://doi.org/10.1002/cctc.202201150> <https://chemistry-europe.onlinelibrary.wiley.com/doi/pdf/10.1002/cctc.202201150>
- [42] Behrens, M., Studt, F., Kasatkin, I., Kühn, S., Hävecker, M., Abild-Pedersen, F., Zander, S., Girgsdies, F., Kurr, P., Kniep, B.-L., Tovar, M., Fischer, R.W., Nørskov, J.K., Schlögl, R.: The active site of methanol synthesis over Cu/ZnO/Al₂O₃ industrial catalysts. *Science* **336**(6083), 893–897 (2012) <https://doi.org/10.1126/science.1219831> <https://www.science.org/doi/pdf/10.1126/science.1219831>
- [43] Studt, F., Sharafutdinov, I., Abild-Pedersen, F., Elkjær, C.F., Hummelshøj, J.S., Dahl, S., Chorkendorff, I., Nørskov, J.K.: Discovery of a Ni-Ga catalyst for carbon

- dioxide reduction to methanol. *Nature Chemistry* **6**(4), 320 (2014) <https://doi.org/10.1038/NCHEM.1873>
- [44] Tang, X., Song, C., Li, H., *et al.*: Thermally stable ni foam-supported inverse CeAlO_x/Ni ensemble as an active structured catalyst for CO₂ hydrogenation to methane. *Nat Commun* **15**(3115), 3115 (2024) <https://doi.org/10.1038/s41467-024-47403-4>
- [45] Hu, F., Ye, R., Lu, Z.-H., Zhang, R., Feng, G.: Structure–activity relationship of Ni-based catalysts toward CO₂ methanation: Recent advances and future perspectives. *Energy & Fuels* **36**(1), 156–169 (2022) <https://doi.org/10.1021/acs.energyfuels.1c03645> <https://doi.org/10.1021/acs.energyfuels.1c03645>
- [46] Kresse, G., Hafner, J.: Ab initio molecular-dynamics simulation of the liquid-metal–amorphous-semiconductor transition in germanium. *Phys. Rev. B* **49**, 14251–14269 (1994) <https://doi.org/10.1103/PhysRevB.49.14251>
- [47] Kresse, G., Furthmüller, J.: Efficient iterative schemes for ab initio total-energy calculations using a plane-wave basis set. *Phys. Rev. B* **54**, 11169–11186 (1996) <https://doi.org/10.1103/PhysRevB.54.11169>
- [48] Mathew, K., Montoya, J.H., Faghaninia, A., Dwarakanath, S., Aykol, M., Tang, H., Chu, I.-h., Smidt, T., Bocklund, B., Horton, M., Dagdelen, J., Wood, B., Liu, Z.-K., Neaton, J., Ong, S.P., Persson, K., Jain, A.: Atomate: A high-level interface to generate, execute, and analyze computational materials science workflows. *Computational Materials Science* **139**, 140–152 (2017) <https://doi.org/10.1016/j.commatsci.2017.07.030>
- [49] Ong, S.P., Richards, W.D., Jain, A., Hautier, G., Kocher, M., Cholia, S., Gunter, D., Chevrier, V.L., Persson, K.A., Ceder, G.: Python materials genomics (pymatgen): A robust, open-source python library for materials analysis. *Computational Materials Science* **68**, 314–319 (2013) <https://doi.org/10.1016/j.commatsci.2012.10.028>
- [50] Ong, S.P., Richards, W.D., Jain, A., Hautier, G., Kocher, M., Cholia, S., Gunter, D., Chevrier, V.L., Persson, K.A., Ceder, G.: Python materials genomics (pymatgen): A robust, open-source python library for materials analysis. *Computational Materials Science* **68**, 314–319 (2013) <https://doi.org/10.1016/j.commatsci.2012.10.028>
- [51] Jain, A., Ong, S.P., Chen, W., Medasani, B., Qu, X., Kocher, M., Brafman, M., Petretto, G., Rignanese, G.-M., Hautier, G., Gunter, D., Persson, K.A.: Fireworks: a dynamic workflow system designed for high-throughput applications. *Concurrency and Computation: Practice and Experience* **27**(17), 5037–5059 (2015) <https://doi.org/10.1002/cpe.3505> <https://onlinelibrary.wiley.com/doi/pdf/10.1002/cpe.3505>

- [52] Gasteiger, J., Shuaibi, M., Sriram, A., Günemann, S., Ulissi, Z., Zitnick, C.L., Das, A.: GemNet-OC: Developing Graph Neural Networks for Large and Diverse Molecular Simulation Datasets (2022). <https://arxiv.org/abs/2204.02782>
- [53] Virtanen, P., Gommers, R., Oliphant, T.E., Haberland, M., Reddy, T., Cournapeau, D., Burovski, E., Peterson, P., Weckesser, W., Bright, J., van der Walt, S.J., Brett, M., Wilson, J., Millman, K.J., Mayorov, N., Nelson, A.R.J., Jones, E., Kern, R., Larson, E., Carey, C.J., Polat, İ., Feng, Y., Moore, E.W., VanderPlas, J., Laxalde, D., Perktold, J., Cimrman, R., Henriksen, I., Quintero, E.A., Harris, C.R., Archibald, A.M., Ribeiro, A.H., Pedregosa, F., van Mulbregt, P., SciPy 1.0 Contributors: SciPy 1.0: Fundamental Algorithms for Scientific Computing in Python. *Nature Methods* **17**, 261–272 (2020) <https://doi.org/10.1038/s41592-019-0686-2>
- [54] Müllner, D.: Modern hierarchical, agglomerative clustering algorithms (2011). <https://arxiv.org/abs/1109.2378>
- [55] Bar-Joseph, Z., Gifford, D.K., Jaakkola, T.S.: Fast optimal leaf ordering for hierarchical clustering. *Bioinformatics* **17**(1), 22–29 (2001) https://doi.org/10.1093/bioinformatics/17.suppl_1.S22 https://academic.oup.com/bioinformatics/article-pdf/17/suppl_1/S22/50522365/bioinformatics_17_suppl1_s22.pdf

Supplementary Information for: Machine-learning Accelerated Descriptor Design for Catalyst Discovery: A CO₂ to Methanol Conversion Case Study

Prajwal Pisal¹, Ondřej Krejčí¹, and Patrick Rinke^{1,2,3,4}

¹*Department of Applied Physics, Aalto University, P.O. Box 11000, AALTO, FI-00076, Finland*

²*Department of Physics, Technical University of Munich, James-Franck-Strasse 1, Garching, 85748, Germany*

³*Atomistic Modeling Center, Munich Data Science Institute, Technical University of Munich, Walther-Von-Dyck Str. 10, Garching, 85748, Germany*

⁴*Munich Center for Machine Learning (MCML)*

December 19, 2024

Corresponding author: patrick.rinke@aalto.fi

Content

Table S1 – All 159 materials used in final evaluation; Table S2 – All materials removed from the final evaluation; Figure S1 – Adsorption energy distributions and hierarchical clustering of all 159 materials; Table S3 – Statistical analysis on the AEDs for a subset of materials shown in Fig. 3 in the main text.

arXiv:2412.13838v1 [physics.chem-ph] 18 Dec 2024

Table S1: All 159 individual metals and bimetallic alloys (M), along with their respective Materials Project IDs (mp-ID) with calculated AEDs having an estimated mean absolute error (EMAE) of less than 0.25 eV. For clarity, the ‘mp-’ portion of the ID has been omitted.

M	mp-ID	M	mp-ID	M	mp-ID	M	mp-ID
Co2	54	GaPd2	1869	Pt	126	YAg	2474
Co3Ni	1008349	GaPt	1025551	V2Ga5	20405	YAg2	999544
Co6Ni2	1183837	GaPt3	862621	V3Au	839	YAu	1066254
CoPt	949	GaRh	2444	V3Fe	1079399	YAu2	1018113
CoPt3	922	In2Ag	19974	V3Ga	22568	YAu3	1079467
CoZn13	30568	In2Au	22154	V3Ir	2006	YCu2	2698
Cu	30	In2Au3	1017579	V3Ni	7226	YCu5	2797
Cu10Zn16	1368	In2Pt	22682	V3Pd	1664	YFe5	11385
Cu3Au	2258	In3Co	22236	V3Pt	2211	YGa2	1914
Cu3Pd	672265	In3Ir	636498	V3Rh	1578	YIn	22704
Cu3Pt	12086	In3Ni2	21385	V4Zn5	30883	YIn3	20131
CuAu	522	In3Pd2	510437	V6Ga5	571557	YIr	30746
CuPd	1018029	In3Pd5	22146	VIr	569250	YIr2	2762
CuPt	644311	In3Rh	18614	VNi3	171	YNi	1364
CuPt7	12608	In4Ag9	21975	VPd2	11549	YNi5	2152
CuZn	987	In7Pd3	568655	VPd3	568711	YPd	1066136
Fe3Ga	19870	InAg3	30343	VPt	2678	YPd3	559
FeNi	2213	InPd2	22646	VPt2	12108	YPt	1025448
FeNi3	1418	InPd3	1078721	VPt3	372	YPt2	2674
FePd3	21845	InPt3	20516	VPt8	1079997	YPt3	2403
FePt	2260	InRh	899	VRh	971751	YRh	191
FeZn13	1722	K	58	VRu	1395	YRh2	921
Ga12Fe4	636368	KAu2	30401	Y2Au	979911	YRh3	1191413
Ga2Au	2776	KAu5	1298	Y2Co17	1106140	YRu2	568186
Ga2Cu	11359	KIn4	22481	Y2In	21294	YZn	2516
Ga2Pt	22095	MnGa4	1069288	Y2Pt	1102657	YZn12	30886
Ga2Ru	1072429	MnNi3	11501	Y2Zn17	17639	YZn3	30884
Ga3Ni5	11398	MnPd3	31138	Y3Co	1105598	Zn11Ir2	30747
Ga3Ru	672204	MnPt3	1180	Y3In5	1105835	Zn11Rh2	13448
Ga4	142	MnV	316	Y3Ir	1207785	Zn2	79
Ga7Pd3	1106289	MnZn13	1210567	Y3Ni	1105633	Zn3Au	30424
Ga7Pt3	1188512	MnZn3	11504	Y3Pd	1207777	Zn3Ru	1380
Ga9Rh2	31312	Ni	23	Y3Pd4	1104019	ZnAg	1912
GaAg2	578	Ni13Ga9	21589	Y3Pt	7343	ZnAu	1684
GaAu	30379	Ni2Ga3	11397	Y3Rh	1207780	ZnPd	1652
GaCo	1121	Ni2Zn2	429	Y3Ru	1207781	ZnPd2	1103252
GaCu3	1183995	Ni3Pt	12798	Y3Zn11	1103536	ZnPt	894
GaIr	11388	Ni4Zn22	11532	Y5Ir2	1104365	ZnPt3	30856
GaNi3	815	Ni6Ga14	16852	Y5Ir3	1198712	ZnRh	6938
GaPd	1078526	NiZn	1486	Y7Rh3	1189474		

Table S2: Materials excluded from the evaluation: A total of 57 individual metals and bimetallic alloys (M), along with their Materials Project ID (mp-ID) and the reason for exclusion (R). The reasons include: B – excessively high estimated MAE; C – too large systems leading to memory overflow; and D – errors during bulk optimization. For simplicity, the ‘mp-’ prefix has been omitted from the IDs.

M	mp-ID	R	M	mp-ID	R	M	mp-ID	R
FeCo	2090	B	MnPd2	1102640	B	K17In41	640781	D
FePt3	649	B	MnPt	1670	B	K2Au3	8700	D
FeRh	1918	B	MnRh	417	B	K8In11	582929	D
Ga2Ir	31253	B	VAu4	1069697	B	NiPt	945	D
Ga4Cu9	1197621	B	VZn3	11578	B	V3Co	1585	D
Ga9Ir2	31311	B	Y5Ru2	1104898	B	V8Ga41	21965	D
In2Ir	22812	B	YFe2	1570	B	VNi2	11531	D
In3Au10	510099	B	YGa	11420	B	Y15Ni32	1200338	D
In3Ru	607450	B	Zn18Fe8	1207450	B	Y2Ni7	574339,	D
K2Pt	1062676	B	Zn22Co4	1192361	B	Y3Ga2	1204352	D
K3Ga9	181	B	Ga17Rh10	30665	C	Y3Ni2	582134	D
Mn3Pd5	1078895	B	Ga2Pd5	405	C	Y3Rh2	1196999	D
Mn6Co2	1185970	B	Ga5Pd13	31485	C	YCo2	1294,	D
MnAu	12674	B	GaPt2	2223	C	YFe3	1102392,	D
MnAu2	11252	B	In7Cu10	646039	C	YNi3	569196,	D
MnAu4	12565	B	ZnAu3	669566	C	YZn5	30885	D
MnCo	1009133	B	Ga5Pt	1199016,	D	Zn13Rh	13447	D
MnGa	1001836	B	In2Pt3	510439	D	Zn49Pt29	569514	D
MnIr	2728	B	InNi	19876	D	Zn6Ru	1205290	D

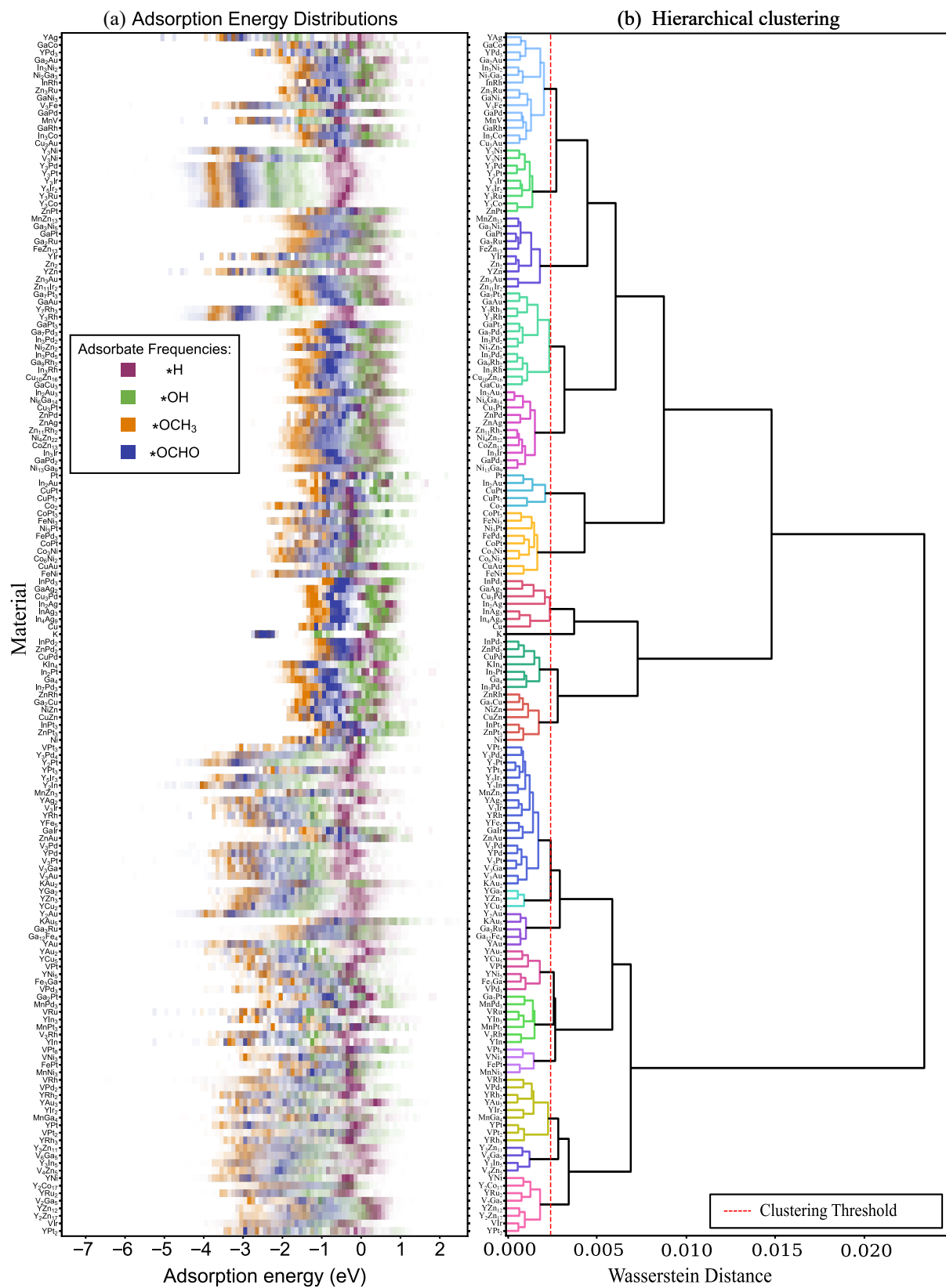


Figure S1: Computation for all 159 materials: (a) Adsorption energy distributions (AEDs) and (b) hierarchical clustering of materials based on pairwise Wasserstein distances between AEDs of all materials.

Table S3: The statistical analysis conducted on the AEDs for a subset of materials (M) depicted in Fig. 3 of the main text. For simplicity, the ‘mp-’ prefix from the Materials Project ID (mp-ID) has been omitted. In the expression $E_{\text{ads}}^{\text{std}}$, **std** denotes the standard deviation. A comprehensive statistical analysis encompassing all 159 materials is available in [1].

Adsorbate		*H					*OCHO				
M	mp-ID	$E_{\text{ads}}^{\text{min}}$	$E_{\text{ads}}^{\text{max}}$	$E_{\text{ads}}^{\text{mean}}$	$E_{\text{ads}}^{\text{median}}$	$E_{\text{ads}}^{\text{std}}$	$E_{\text{ads}}^{\text{min}}$	$E_{\text{ads}}^{\text{max}}$	$E_{\text{ads}}^{\text{mean}}$	$E_{\text{ads}}^{\text{median}}$	$E_{\text{ads}}^{\text{std}}$
InPd ₃	1078721	-0.54	1.29	-0.13	-0.22	0.32	-1.04	0.35	-0.52	-0.58	0.22
GaAg ₂	578	0.22	1.05	0.46	0.45	0.13	-1.06	0.68	-0.61	-0.65	0.23
Cu ₃ Pd	672265	-0.17	0.52	-0.01	-0.06	0.14	-1.05	0.09	-0.76	-0.86	0.24
In ₂ Ag	19974	0.27	1.35	0.59	0.58	0.13	-0.96	-0.08	-0.71	-0.72	0.13
InAg ₃	30343	0.24	1.07	0.47	0.43	0.15	-0.88	0.11	-0.59	-0.64	0.20
In ₄ Ag ₉	21975	0.12	0.98	0.45	0.44	0.15	-0.93	0.41	-0.63	-0.65	0.19
Cu	30	-0.14	0.49	0.01	-0.03	0.14	-1.29	-0.15	-0.89	-0.93	0.32
K	58	-0.01	1.00	0.15	0.09	0.19	-2.81	-2.30	-2.57	-2.60	0.14
InPd ₂	22646	-0.39	1.20	-0.03	-0.14	0.27	-1.09	0.71	-0.62	-0.65	0.25
ZnPd ₂	1103252	-0.38	0.81	-0.13	-0.17	0.20	-1.11	0.77	-0.53	-0.57	0.28
CuPd	1018029	-0.44	0.72	-0.20	-0.23	0.21	-1.12	0.25	-0.59	-0.62	0.31
KIn ₄	22481	-0.40	1.87	0.34	0.31	0.21	-2.36	-0.33	-1.36	-1.37	0.26
In ₂ Pt	22682	-0.33	1.72	0.20	0.03	0.35	-1.69	0.07	-0.85	-0.86	0.29
Ga ₄	142	-0.71	1.15	0.27	0.26	0.28	-1.73	-0.07	-0.97	-0.98	0.26
In ₇ Pd ₃	568655	-0.36	1.02	0.36	0.35	0.22	-1.20	0.18	-0.80	-0.83	0.18
ZnRh	6938	-0.63	0.89	-0.29	-0.37	0.32	-1.39	0.01	-0.92	-1.03	0.33
Ga ₂ Cu	11359	-0.20	1.27	0.28	0.24	0.24	-1.36	0.19	-0.86	-0.87	0.30
NiZn	1486	-0.49	1.08	-0.14	-0.24	0.33	-1.81	0.12	-1.11	-1.16	0.37
CuZn	987	-0.19	1.02	0.17	0.15	0.19	-1.67	-0.12	-1.03	-1.12	0.33
InPt ₃	20516	-0.59	1.34	-0.22	-0.28	0.34	-1.09	0.47	-0.44	-0.45	0.34
ZnPt ₃	30856	-0.43	0.99	-0.19	-0.20	0.20	-0.98	0.66	-0.37	-0.32	0.37
Ni	23	-0.53	0.14	-0.37	-0.42	0.16	-1.66	-0.11	-1.06	-1.09	0.41
Y ₃ Zn ₁₁	1103536	-0.89	0.86	-0.17	-0.18	0.24	-3.92	0.36	-2.06	-2.07	0.60
V ₆ Ga ₅	571557	-1.30	1.08	-0.53	-0.66	0.38	-5.44	0.00	-2.06	-1.99	0.65
Y ₃ In ₅	1105835	-0.88	1.11	-0.16	-0.11	0.36	-4.61	0.50	-2.45	-2.38	0.80
V ₄ Zn ₅	30883	-1.13	0.96	-0.44	-0.42	0.44	-3.72	0.30	-2.08	-2.15	0.53
Adsorbate		*OH					*OCH ₃				
M	mp-ID	$E_{\text{ads}}^{\text{min}}$	$E_{\text{ads}}^{\text{max}}$	$E_{\text{ads}}^{\text{mean}}$	$E_{\text{ads}}^{\text{median}}$	$E_{\text{ads}}^{\text{std}}$	$E_{\text{ads}}^{\text{min}}$	$E_{\text{ads}}^{\text{max}}$	$E_{\text{ads}}^{\text{mean}}$	$E_{\text{ads}}^{\text{median}}$	$E_{\text{ads}}^{\text{std}}$
InPd ₃	1078721	0.27	1.16	0.60	0.58	0.14	-1.22	-0.38	-0.90	-0.92	0.13
GaAg ₂	578	-0.25	1.21	0.24	0.16	0.25	-1.80	-0.32	-1.28	-1.35	0.25
Cu ₃ Pd	672265	-0.04	0.90	0.24	0.18	0.22	-1.53	-0.64	-1.21	-1.27	0.21
In ₂ Ag	19974	-0.06	0.88	0.23	0.21	0.16	-1.59	-0.59	-1.27	-1.29	0.16
InAg ₃	30343	0.09	0.93	0.42	0.45	0.21	-1.41	-0.54	-1.07	-1.05	0.20
In ₄ Ag ₉	21975	-0.07	1.12	0.38	0.33	0.20	-1.53	-0.42	-1.14	-1.19	0.20
Cu	30	-0.18	0.76	0.12	0.09	0.24	-1.64	-0.82	-1.40	-1.46	0.19
K	58	-1.31	-0.10	-1.14	-1.20	0.19	-2.77	-1.72	-2.59	-2.65	0.16
InPd ₂	22646	-0.04	1.13	0.46	0.45	0.20	-1.57	-0.33	-1.04	-1.06	0.19
ZnPd ₂	1103252	0.06	1.16	0.53	0.54	0.22	-1.44	-0.30	-0.97	-0.96	0.20
CuPd	1018029	0.03	1.07	0.48	0.45	0.24	-1.41	-0.42	-0.97	-0.99	0.23
KIn ₄	22481	-1.11	0.47	-0.35	-0.36	0.21	-2.46	-0.64	-1.80	-1.83	0.25
In ₂ Pt	22682	-0.54	1.00	0.09	0.21	0.41	-2.12	-0.55	-1.41	-1.30	0.40
Ga ₄	142	-0.98	0.23	-0.24	-0.21	0.20	-2.36	-1.02	-1.73	-1.72	0.20
In ₇ Pd ₃	568655	-0.33	1.00	0.17	0.16	0.23	-1.80	-0.61	-1.34	-1.36	0.23
ZnRh	6938	-0.30	0.93	0.18	0.12	0.23	-1.71	-0.85	-1.37	-1.42	0.20
Ga ₂ Cu	11359	-0.92	0.72	-0.02	-0.06	0.23	-2.06	-0.85	-1.54	-1.57	0.22
NiZn	1486	-0.49	0.63	-0.09	-0.21	0.24	-1.93	-1.05	-1.57	-1.62	0.22
CuZn	987	-0.44	0.77	-0.05	-0.11	0.24	-1.94	-0.96	-1.55	-1.57	0.22
InPt ₃	20516	0.13	1.92	0.66	0.65	0.23	-1.41	-0.25	-0.90	-0.93	0.22
ZnPt ₃	30856	0.10	1.31	0.59	0.56	0.27	-1.40	-0.33	-0.97	-1.02	0.24
Ni	23	-0.54	0.57	-0.08	-0.16	0.29	-2.05	-0.80	-1.65	-1.66	0.27
Y ₃ Zn ₁₁	1103536	-2.22	0.51	-1.16	-1.27	0.52	-3.68	-0.51	-2.69	-2.83	0.53
V ₆ Ga ₅	571557	-3.37	0.65	-1.21	-1.29	0.53	-3.78	-0.92	-2.80	-2.93	0.52
Y ₃ In ₅	1105835	-2.51	0.48	-1.50	-1.59	0.67	-3.93	-0.97	-2.99	-3.15	0.64
V ₄ Zn ₅	30883	-2.29	0.37	-1.29	-1.46	0.64	-3.87	-1.10	-2.84	-3.02	0.66

References

- [1] P. Písal and O. Krejčí. DATASET: Final geometries and energies, statistical analysis and estimated errors of single metals and bimetallics for CO₂ to methanol conversion, Aug. 2024. Zenodo, <https://doi.org/10.5281/zenodo.13370374>.